

Stellar Surface Density Modulates Mg II Cool-gas Outflow Absorption in DESI Star-forming Galaxies

YU RONG^{1,2} AND SHIHONG LIU^{1,2}

¹*Department of Astronomy, University of Science and Technology of China, Hefei, Anhui 230026, China*

²*School of Astronomy and Space Sciences, University of Science and Technology of China, Hefei 230026, Anhui, China*

ABSTRACT

Galaxy outflows are usually ordered by stellar mass and star-formation rate (SFR), but the same feedback budget may couple differently to gas in diffuse and compact galaxies. We use Dark Energy Spectroscopic Instrument (DESI) Data Release 1 stacked spectra of massive star-forming galaxies at $0.35 < z < 1.0$ to test whether stellar surface density, $\Sigma_* = M_*/(2\pi R_e^2)$, is an independent empirical coordinate of down-the-barrel singly ionized magnesium (Mg II) cool-gas absorption. In AGN-clean samples matched in stellar mass, and in a stricter sample matched in both stellar mass and a Balmer-line SFR proxy, the Mg II outflow equivalent width (EW) rises monotonically with Σ_* in every redshift bin. From the lowest to highest Σ_* tertile, EW_{out} increases by 0.37–0.61 Å, while the absolute outflow velocity changes only weakly. DESI therefore shows that cool-gas outflow strength in massive star-forming galaxies is not set only by how much stellar mass or star formation a galaxy has, but also by how tightly the galaxy is built. The structural dependence points to changes in the absorbing velocity distribution and/or the effective covering fraction of cool outflowing gas.

Keywords: galaxies: evolution — galaxies: ISM — galaxies: star formation — galaxies: kinematics and dynamics — techniques: spectroscopic

1. INTRODUCTION

Galactic winds are a major channel through which stellar feedback regulates galaxy growth, transports metals, and connects the interstellar medium to the circumgalactic medium (e.g., Chevalier & Clegg 1985; Dekel & Silk 1986; Heckman et al. 2000; Veilleux et al. 2005; Rupke et al. 2005; Murray et al. 2005; Oppenheimer & Dave 2006; Muratov et al. 2015; Somerville & Dave 2015; Naab & Ostriker 2017; Veilleux et al. 2020). Observationally, outflows are seen from the nearby Universe to the peak epoch of cosmic star formation through optical emission-line kinematics, Na I absorption, molecular and atomic gas tracers, and rest-frame ultraviolet interstellar absorption (Heckman et al. 2000; Shapley et al. 2003; Martin 2005; Rupke et al. 2005; Steidel et al. 2010; Arribas et al. 2014; Cicone et al. 2014). These measurements provide the empirical basis for the feedback prescriptions used in galaxy-evolution models, but they also show that winds are multi-phase, geometrically complex, and difficult to summarize with a single velocity or mass-loading factor.

The cool, low-ionization phase is important because it contains a large fraction of the entrained neutral gas and metals. In integrated spectra, the down-the-barrel geometry gives a

direct view of this material projected against the galaxy’s own stellar continuum. The Mg II $\lambda\lambda 2796, 2803$ and Fe II transitions are standard tracers of cool outflowing gas at intermediate redshift: they are strong, accessible from the ground over a broad redshift interval, and sensitive to gas at velocities of a few hundred km s^{−1}. Large surveys and deep spectroscopic samples have shown that blueshifted low-ionization absorption is common in star-forming galaxies, and that its incidence, equivalent width, and velocity depend on stellar mass, SFR, luminosity, inclination, and starburst properties (Tremonti et al. 2007; Weiner et al. 2009; Rubin et al. 2010; Martin et al. 2012; Kornei et al. 2012; Erb et al. 2012; Bordoloi et al. 2014; Rubin et al. 2014; Chisholm et al. 2015; Heckman & Borthakur 2016). At the same time, Mg II profiles are not simple linear measures of outflow column density: saturation, partial covering, resonant emission filling, and velocity structure all shape the observed absorption profile (Rubin et al. 2011; Erb et al. 2012; Martin et al. 2013; Rubin et al. 2014).

Most empirical scaling relations have been framed in terms of integrated quantities such as stellar mass, M_* , and star-formation rate, SFR. However, feedback should also depend on how concentrated the stars and star formation are. Compact starbursts can drive unusually fast outflows, suggesting that feedback depends on the spatial arrangement of stars and gas as well as on the integrated star-formation budget (Diamond-Stanic et al. 2012; Sell et al. 2014; Heck-

man & Borthakur 2016). Local starburst work, integral-field-unit (IFU) studies, and high-redshift emission-line measurements have likewise emphasized that large-scale winds are connected to how intensely feedback is concentrated within galaxies (Heckman et al. 2000; Newman et al. 2012; Arribas et al. 2014). These results suggest that total SFR alone is an incomplete feedback coordinate. A galaxy with the same M_* and SFR but a smaller effective radius may couple energy and momentum to cool gas differently, either because the launch region is more compact or because the stellar potential and gas column structure are different.

The relevant structural variable for a large statistical experiment is a surface-density proxy. We use $\Sigma_* = M_*/(2\pi R_e^2)$, where R_e is the effective radius, because it is available for a very large DESI sample and captures the compactness of the stellar body. This choice is complementary to SFR-based wind scalings: M_* sets much of the potential-well scale, SFR traces the instantaneous feedback budget, and Σ_* asks whether the same mass and feedback are arranged in a way that changes the observed cool outflow. Testing this requires both large numbers and controlled comparisons, since Σ_* , M_* , and SFR are mutually correlated in real galaxy samples (Franx et al. 2008; Wuyts et al. 2011; Rong et al. 2020).

The Dark Energy Spectroscopic Instrument (DESI) now provides the sample size needed to make such a differential test. In previous work, stacked DESI spectra have already shown that Mg II outflow equivalent width (EW) is closely linked to SFR while the characteristic velocity is more closely tied to stellar mass (Yu et al. 2025). That result motivates the next structural question: at fixed M_* and SFR, does a more compact galaxy show stronger cool outflowing gas? We address this question with a controlled DESI stacking experiment: in each redshift bin we compare Mg II absorption across Σ_* tertiles after matching the stellar-mass distribution and, in a stricter test, the line-SFR distribution. The resulting measurements provide a benchmark for future observational and theoretical work that asks whether galaxy structure, beyond M_* and SFR, regulates cool-gas feedback.

2. DATA AND SAMPLE

2.1. Catalogs and Basic Cuts

We use DESI Data Release 1 (DR1) coadded spectra (DESI Collaboration et al. 2022, 2025) and the DESI stellar-mass and emission-line value-added catalog of Zou et al. (2024). The catalog uses the official DESI pipeline redshifts; the catalog measurements used in this work are stellar-population quantities, imaging sizes, and emission-line fluxes. We require main-survey galaxies with redshift $0.35 < z < 1.0$, $\log(M_*/M_\odot) > 10.5$, finite positive Legacy Survey size parameter R_e , a valid coadd file, DESI ZWARN= 0, and DESI spectral type ‘GALAXY’, and $|c(z_{\text{catalog}} - z_{\text{DESI}})/(1 + z_{\text{DESI}})| < 100 \text{ km s}^{-1}$, where c is the speed of light, z_{catalog} is the value propagated in the catalog of Zou et al. (2024), and z_{DESI} is the official DESI pipeline redshift. The last cut removes sources with obvious redshift failures before rest-frame stacking.

The stellar surface density is defined as

$$\Sigma_* = \frac{M_*}{2\pi R_e^2}, \quad (1)$$

where R_e is the physical half-light radius inferred from the catalog SHAPE_R measured by the Legacy Surveys imaging model fits (Dey et al. 2019) and converted to kpc using the official DESI redshift. SHAPE_R is the observed half-light/effective radius of the galaxy model in arcsec.

2.2. AGN-clean Selection

We remove possible active galactic nucleus (AGN), composite, low-ionization nuclear emission-line region (LINER)-like, and shock-contaminated systems before stacking. Where H α , H β , [O III] λ 5007, and [N II] λ 6583 have S/N > 3, we use the [N II] Baldwin–Phillips–Terlevich (BPT) diagram and veto sources outside the star-forming sequence (Baldwin et al. 1981; Kauffmann et al. 2003; Kewley et al. 2001). Where [S II] λ λ 6716, 6731 is also measurable, we apply the analogous [S II] BPT veto following the standard optical classification framework (Kewley et al. 2006). At redshifts where the full BPT set is not always available, we additionally remove sources with [Ne V] λ 3346, [Ne V] λ 3426, or He II λ 4686 detected at S/N > 2. Any available indication of non-stellar hard ionization removes the object. This selection is stricter than a completeness-oriented sample, but it yields cleaner star-forming stacks for testing stellar-feedback-driven absorption.

2.3. Redshift and Surface-density Bins

We analyze three redshift bins: $0.35 < z < 0.45$, $0.45 < z < 0.60$, and $0.60 < z < 1.00$. In each redshift bin, the AGN-clean sample is split into tertiles of $\log \Sigma_*$. We construct two controlled samples. In the first, the three Σ_* tertiles are randomly down-sampled in narrow M_* bins to the same mass distribution. This mass-matched sample preserves the observed covariance between Σ_* and SFR. In the second, the tertiles are matched in both M_* and line-SFR using two-dimensional M_* –SFR cells. The line-based SFR is estimated from H β when its signal-to-noise ratio, S/N(H β), is greater than 3, otherwise from H α when S/N(H α) > 3 and the line falls in the DESI wavelength range (Kennicutt & Evans 2012). This sample tests whether a residual Σ_* signal remains after SFR is also fixed.

The per-tertile sample sizes are 51,012, 23,982, and 34,207 for the mass-matched sample, and 46,063, 23,071, and 30,164 for the mass+SFR-matched sample in the three redshift bins. Figure 1 shows that the matching works as intended. In the mass-matched sample the median M_* range across Σ_* tertiles is only 0.0002–0.003 dex, while SFR still shifts systematically with Σ_* . In the mass+SFR-matched sample the median SFR range is also reduced to 0.001–0.006 dex.

3. STACKING AND MEASUREMENTS

Each coadded spectrum is shifted to the rest frame and re-sampled onto a common grid over 2700–2910 Å. We then

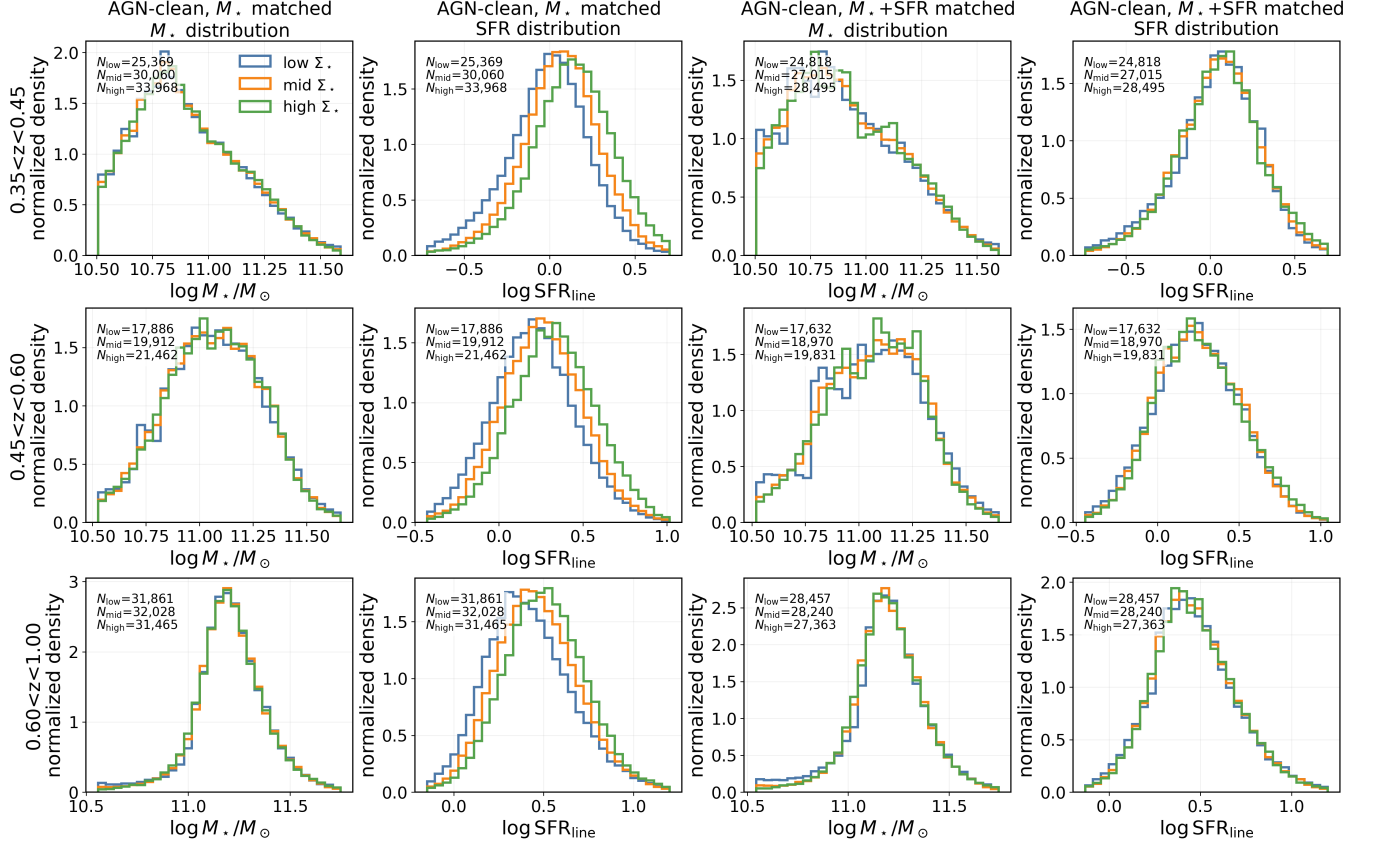


Figure 1. Control distributions for the two final AGN-clean samples. Rows show the three redshift intervals, and colors show the low-, middle-, and high- Σ_* tertiles; the annotated numbers give the final number of galaxies entering each stack. The left two columns show the sample matched in M_* only, preserving the observed covariance between Σ_* and SFR. The right two columns show the sample matched in both M_* and line-SFR.

continuum-normalize each spectrum using the same local-polynomial approach as Yu et al. (2025). Specifically, we mask the strong rest-UV features near Fe II $\lambda\lambda 2586, 2600, \text{Mg II } \lambda\lambda 2796, 2803$, and Mg I $\lambda 2853$, smooth the remaining spectrum with a median filter, fit a fifth-order polynomial to the unmasked pixels, and divide the spectrum by this fitted continuum. Spectra with failed continuum fits or pathological normalizations are discarded. Within each bin we median-stack the normalized spectra with equal galaxy weight; no flux, luminosity, or S/N weighting is applied.

We define the outflow equivalent width, EW_{out} , following Yu et al. (2025). We integrate the Mg II $\lambda 2796$ blue side over $-700 < v_{2796} < 0 \text{ km s}^{-1}$ to obtain $\text{EW}_{\text{blue},2796}$, and the Mg II $\lambda 2803$ red side over $0 < v_{2803} < 400 \text{ km s}^{-1}$ to obtain $\text{EW}_{\text{red},2803}$. The outflow component is then

$$\text{EW}_{\text{out}} = 2(\text{EW}_{\text{blue},2796} - \text{EW}_{\text{red},2803}). \quad (2)$$

$\text{EW}_{\text{red},2803}$ is therefore a reference window for subtracting the non-outflow component, not a doublet-ratio measurement. We compute v_{out} with the same prescription. Let $A(v) = \max[1 - F(v), 0]$ be the positive absorption depth in the two windows, with velocities defined relative to the corresponding doublet component. The absorption-weighted velocity of the two-window profile, evaluated on the rest-frame

wavelength grid, is

$$v_{\text{tot}} = \frac{\int_{-700}^0 v_{2796} A_{2796}(v) d\lambda + \int_0^{400} v_{2803} A_{2803}(v) d\lambda}{\int_{-700}^0 A_{2796}(v) d\lambda + \int_0^{400} A_{2803}(v) d\lambda}. \quad (3)$$

Following Yu et al. (2025), we then define

$$v_{\text{out}} = v_{\text{tot}} \frac{\text{EW}_{\text{tot}}}{\text{EW}_{\text{out}}}, \quad (4)$$

$$\text{EW}_{\text{tot}} = 2(\text{EW}_{\text{blue},2796} + \text{EW}_{\text{red},2803}).$$

The normalization and velocity windows are fixed for all bins. Uncertainties on EW_{out} and v_{out} are estimated with galaxy-level bootstrap resampling. For each of the 18 stacks (two controlled samples, three redshift bins, and three Σ_* tertiles), we resample the contributing galaxies with replacement 200 times, repeat the stack and measurement, and quote the 16th–84th percentile interval.

4. RESULTS

4.1. MgII Outflows Strengthen with Stellar Surface Density

Figure 2 shows the main result. In both controlled samples and all three redshift bins, EW_{out} increases from

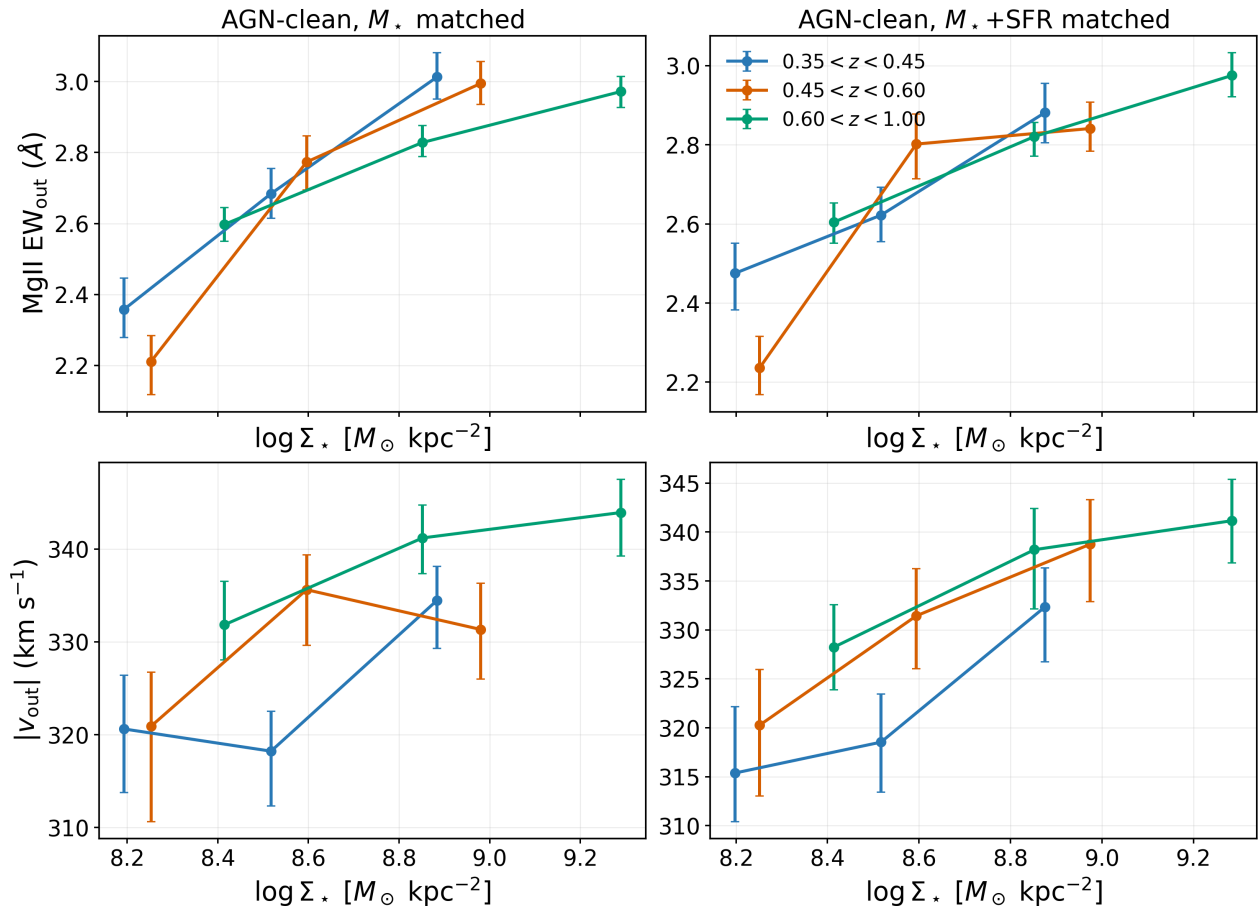


Figure 2. Observed Mg II outflow absorption strength as a function of stellar surface density. Left: AGN-clean stacks matched in M_* . Right: AGN-clean stacks matched in both M_* and SFR. Points show the three Σ_* tertiles in each redshift interval. Error bars are 16th–84th percentile intervals from 200 galaxy-bootstrap realizations per stack. The EW trend remains after controlling both M_* and SFR, while the velocity trend is weaker.

the low- to high- Σ_* tertile. In the mass-matched sample, which preserves the observed SFR- Σ_* covariance, the low-to-high increase is $0.658^{+0.115}_{-0.104}$, $0.792^{+0.091}_{-0.098}$, and $0.373^{+0.062}_{-0.060}$ Å in the three redshift bins, respectively. In the stricter mass+SFR-matched sample, the increase remains $0.413^{+0.113}_{-0.113}$, $0.614^{+0.096}_{-0.098}$, and $0.369^{+0.068}_{-0.067}$ Å in the three redshift bins. Thus the structural trend remains after controlling both M_* and the line-SFR proxy.

The velocity trend is much weaker. In the fiducial mass+SFR-matched sample, $|v_{\text{out}}|$ increases by 15^{+8}_{-7} , 19^{+8}_{-8} , and 12^{+7}_{-6} km s $^{-1}$ from the low- to high- Σ_* tertile. These differences are far smaller than the single-spectrum DESI instrumental width at the observed Mg II wavelengths (tens to more than 100 km s $^{-1}$, depending on camera and redshift), and should not be interpreted as a resolved velocity separation between stacks. The primary result is the EW increase; the velocity change is very small and may not be trusted.

4.2. What Drives the EW Trend?

Figure 3 shows two non-parametric profile-shape diagnostics used to interpret the EW trend. Absorption-line studies commonly use residual depth, equivalent width, absorption-

weighted velocity, maximum velocity, and line width to describe outflow profiles and their velocity distributions (e.g., Martin 2005; Weiner et al. 2009; Chisholm et al. 2015, 2016). For our stacked spectra we use percentile versions of these quantities, which are less sensitive to individual noisy pixels than extrema or single-pixel depths. Let $F(v)$ be the continuum-normalized stacked flux as a function of velocity v relative to Mg II $\lambda 2796$, and define the positive absorption profile $D(v) = \max[1 - F(v), 0]$. Over $-700 < v < -50$ km s $^{-1}$, we define the blue-wing depth as $1 - P_{10}[F(v)]$, where P_{10} is the 10th percentile of the normalized flux. We define width_{90} as the difference between the 95th and 5th percentiles of the velocity distribution weighted by $D(v)$ over the same interval. Thus width_{90} is a robust measure of the velocity range occupied by the absorbing gas, analogous to the line-width and v_{90} -type quantities used in UV absorption-line outflow work (Chisholm et al. 2015, 2016).

For a continuum-normalized resonant absorption profile, the residual flux can be written schematically as

$$F(v) \simeq 1 - C_f(v) \left[1 - e^{-\tau(v)} \right] + F_{\text{em}}(v), \quad (5)$$

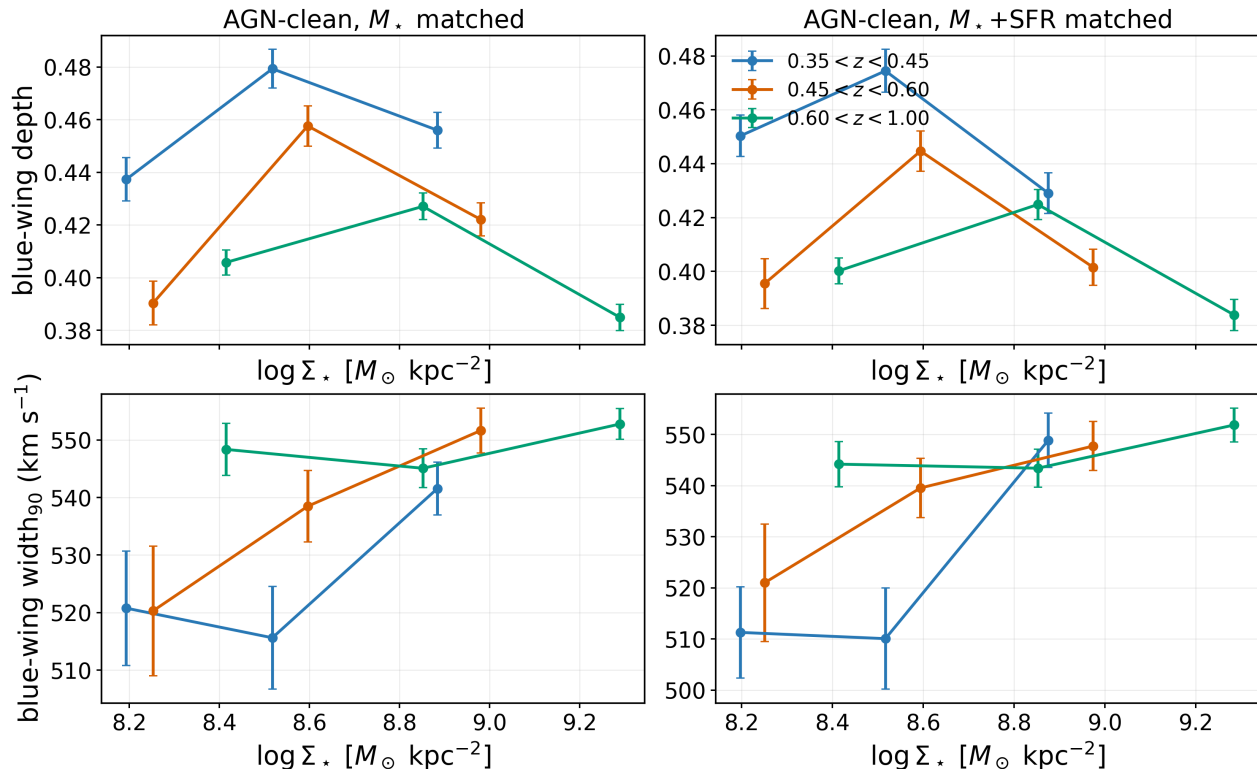


Figure 3. Profile-shape diagnostics for the EW_{out} trend shown in Figure 2. From top to bottom: blue-wing absorption depth $1 - P_{10}[F(v)]$ and blue-wing velocity width width_{90} . Error bars are Monte Carlo uncertainties from the stacked-spectrum error arrays. The depth trend is not monotonic, while width_{90} generally increases with Σ_* .

where $C_f(v)$ is the covering fraction of absorbing gas, $\tau(v)$ is the optical depth, and $F_{\text{em}}(v)$ represents resonantly scattered emission that fills the trough. This standard degeneracy means that the same EW can arise from a larger column density, larger covering fraction, weaker emission filling, or absorption extending over more velocities (e.g., Rubin et al. 2011; Erb et al. 2012; Martin et al. 2012, 2013; Rubin et al. 2014; Chisholm et al. 2015).

The blue-wing absorption depth does not increase monotonically with Σ_* , as shown in the upper panels of Fig. 3. If the EW trend were driven only by increasing covering fraction at fixed velocity structure and emission filling, the trough would deepen systematically. The observed depth behavior disfavors that simplest interpretation.

In contrast, width_{90} generally increases with Σ_* , as shown in the lower panels of Fig. 3. In the mass+SFR-matched sample, the low-to-high changes are about 38, 27, and 8 km s^{-1} in the three redshift bins. Since the EW increases without a monotonic increase in trough depth, the additional absorbed area is most naturally associated with absorption spread over a wider range of velocities, possibly combined with changes in velocity-dependent covering fraction or emission filling.

5. DISCUSSION

5.1. Why AGN-clean Samples Are the Appropriate Test

The AGN-clean selection is designed to isolate star-formation-driven absorption. The AGN/composite fraction

can increase with M_* , compactness, and Σ_* ; retaining such objects could therefore produce an apparent $\text{EW}_{\text{out}}-\Sigma_*$ relation unrelated to stellar feedback. The trend persists after BPT, [Ne V], and He II vetoes, and is already present in the lowest redshift bin where the optical BPT classification is most complete.

5.2. Comparison with Previous MgII Work

Our result complements the DESI Mg II census of Yu et al. (2025). They showed that cool outflow equivalent width depends strongly on SFR and that velocity is linked to stellar mass. We explicitly control both quantities and find a remaining dependence on Σ_* . A natural interpretation is that total star formation sets much of the absorbing-gas strength, stellar mass sets part of the velocity scale, and compactness controls how efficiently feedback couples to cool gas at fixed mass and SFR.

The interpretation is consistent with earlier down-the-barrel absorption work showing that Mg II absorption strength mixes covering fraction, velocity spread, saturation, and resonant emission filling (e.g., Martin 2005; Weiner et al. 2009; Rubin et al. 2014). It is also consistent with the DESI Mg II analysis of Yu et al. (2025). Because Mg II is a resonant transition, an increase in EW_{out} can reflect absorbing gas covering more velocity space, a larger effective covering fraction, different emission filling, or some combination of these effects.

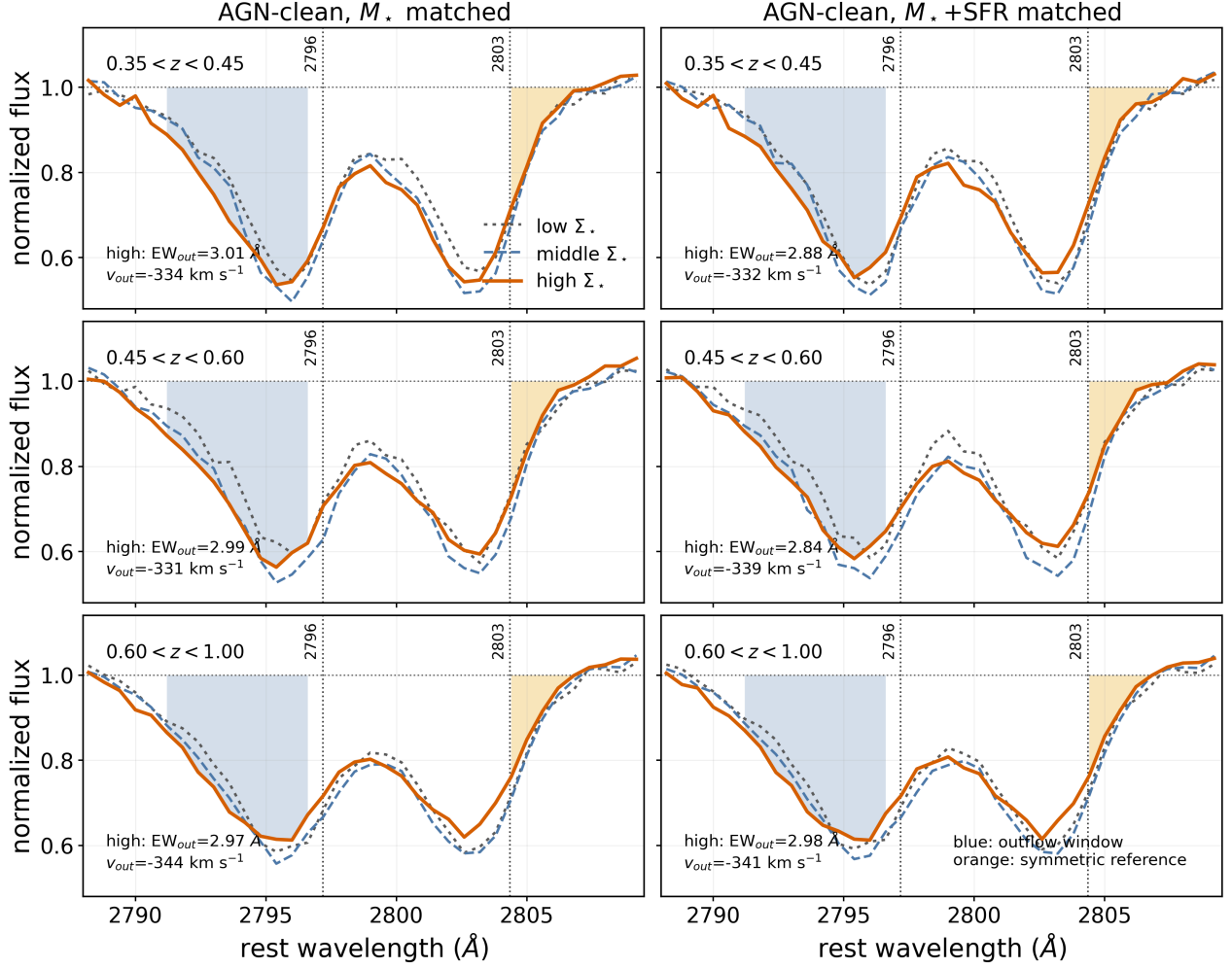


Figure 4. Stacked Mg II doublet profiles for the two controlled samples. Line style denotes Σ_* tertile. The vertical dotted lines mark the rest wavelengths of Mg II λ 2796 and Mg II λ 2803. The blue shaded region marks the blueshifted outflow window for the high- Σ_* stack, while the orange shaded region marks the red-side symmetric reference window used to estimate the non-outflow component. The stronger high- Σ_* absorption is visible directly in the blue wing.

5.3. Physical Picture

At fixed M_* and SFR, increasing Σ_* means the same stellar mass is packed into a smaller projected radius. In real galaxies this structural coordinate can trace several coupled physical conditions: a more compact stellar potential, a different gas column structure, and more concentrated feedback sites. The observed response is a larger absorption EW with a broader blue wing. High- Σ_* galaxies therefore appear to place cool gas over a wider range of outflow velocities and/or cover a larger effective fraction of the stellar continuum.

Dust reddening has little effect on the locally continuum-normalized absorption profile, though it can affect the SFR proxy used for matching. Inclination and morphology may add scatter to down-the-barrel absorption strengths. Full radiative-transfer modeling would be required to convert the empirical depth and width diagnostics into unique covering fractions, velocity fields, and column densities.

5.4. Robustness of the Structural Trend

The two controlled samples test different aspects of the same trend. The M_* -matched sample keeps the observed covariance between surface density and star formation. The M_* +SFR-matched sample tests for a residual structural signal after removing that covariance. The EW_{out} trend is present in both.

The bootstrap uncertainties show that the EW_{out} increase is much more significant than the velocity increase. In the mass+SFR-matched stacks, the low-to-high- Σ_* EW differences are positive at 3.7 – 6.3σ if the 16th–84th percentile half-widths are treated as Gaussian errors, whereas the corresponding velocity differences are weak. The same statement holds in the M_* -matched stacks, where the EW increase is significant at 5.8 – 7.6σ . The first two redshift bins, where the median redshift range across Σ_* tertiles is only 0.001 – 0.010 , show the strongest EW trends; the broader $0.60 < z < 1.00$ bin also shows a positive trend. Thus the result is not driven by a single redshift interval or by the broadest high-redshift bin.

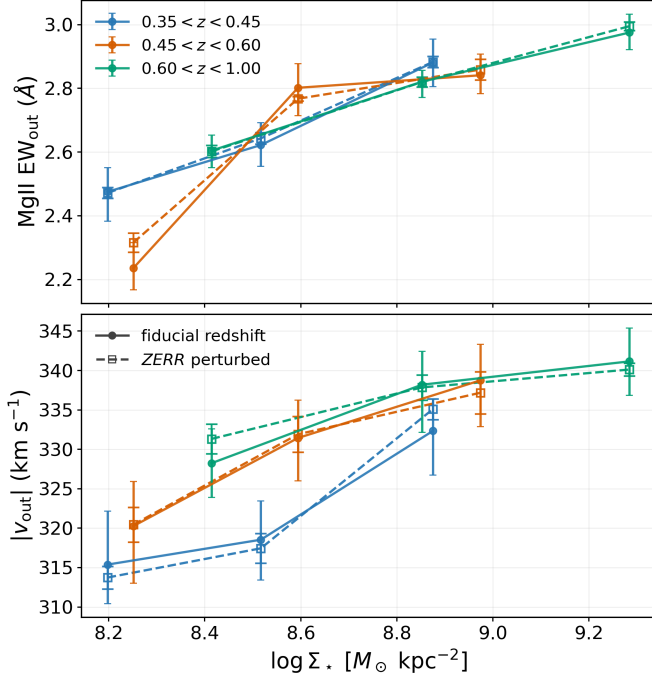


Figure 5. Test of statistical DESI redshift errors for the M_* +SFR-matched sample. Circles show the fiducial stacks using the official DESI redshifts, and squares show stacks after perturbing each galaxy by its catalog redshift uncertainty before rest-frame stacking. The low-to-high- Σ_* EW_{out} trend is unchanged within the redshift-perturbation scatter.

The redshift cut, $|c\Delta z/(1+z)| < 100 \text{ km s}^{-1}$ with $\Delta z = z_{\text{catalog}} - z_{\text{DESI}}$, limits artificial profile broadening from catastrophic redshift mistakes before stacking. Because the normalized spectra are median-stacked with equal galaxy weight, the measurement is not luminosity weighted. The galaxy-level bootstrap tests the sensitivity of each stack to the finite set of contributing galaxies.

We also tested the effect of the statistical DESI redshift uncertainty on the most restrictive M_* +SFR-matched sample. For each contributing galaxy, we perturbed the official DESI redshift by a Gaussian deviate with standard deviation equal to the catalog redshift uncertainty, shifted the spectrum to the perturbed rest frame, repeated the stack, and remeasured the Mg II quantities. Figure 5 compares these redshift-perturbed stacks with the fiducial stacks. The effect is small. The perturbed low-to-high Σ_* EW_{out} increases are 0.41 ± 0.01 , 0.54 ± 0.05 , and $0.39 \pm 0.03 \text{ \AA}$ in the three redshift bins, consistent with the fiducial increases of 0.41, 0.61, and 0.37 \AA . The corresponding changes in $|v_{\text{out}}|$ are only a few km s^{-1} . Thus the statistical redshift uncertainty broadens the profiles slightly but does not erase the $\text{EW}_{\text{out}}-\Sigma_*$ trend.

The DESI line-spread function (LSF) is another relevant limitation for stacked Mg II profiles. The LSF varies with observed wavelength and therefore with redshift for a fixed rest-frame feature; stacking spectra over a redshift range also combines galaxies with different instrumental broadening.

The main quantity in this paper, EW_{out} , is a broad-window integral of the continuum-normalized absorption profile. A normalized LSF primarily redistributes absorption area in wavelength, and therefore should not dominate an EW measurement when the continuum normalization is reliable and the measurement window is wide enough to include the trough. The effect is more important for detailed profile-shape quantities, because LSF smoothing broadens and shallows absorption features.

For this reason, and to keep the measurement directly comparable to the empirical DESI Mg II stacking analysis of Yu et al. (2025), our fiducial stacks do not deconvolve individual spectra or convolve all spectra to a common rest-frame LSF. Yu et al. (2025) likewise treated the DESI LSF as an interpretive limitation on stacked Mg II profile shapes rather than as a fiducial correction to the stacked spectra. In our analysis, quantities that depend on detailed profile shape, especially v_{out} , depth, and width_{90} , should therefore be interpreted as observed stacked-profile measurements rather than intrinsic gas-velocity widths.

We nevertheless performed an explicit test to evaluate the possible LSF impact on our structural trends. For each contributing spectrum, we estimated the DESI resolution at the observed Mg II wavelength, converted it to the rest frame, convolved the locally normalized rest-frame spectrum to a common rest-frame Gaussian width of $\sigma_{\text{LSF}} = 2.0 \text{ \AA}$, and repeated the stacking and EW measurement. We then remeasured EW_{out} , blue-wing depth, and width_{90} in the common-LSF stacks. Figure 6 compares the fiducial and common-LSF measurements. The common-LSF smoothing lowers the absolute EW_{out} values, as expected for fixed finite measurement windows, but the structural trend remains. In the M_* -matched stacks, the low-to-high Σ_* EW_{out} increases are 0.60, 0.66, and 0.46 \AA in the three redshift bins. In the M_* +SFR-matched stacks, the corresponding increases are 0.39, 0.55, and 0.41 \AA . Thus the $\text{EW}_{\text{out}}-\Sigma_*$ relation is not produced by redshift-dependent DESI resolution.

The LSF test also leaves the qualitative profile interpretation unchanged. After common-LSF smoothing, the blue-wing depth still does not provide a simple monotonic explanation for the EW trend, while width_{90} increases from the low- to high- Σ_* tertile in all three redshift bins for both controlled samples. The common-LSF width_{90} increases are 9–13 km s^{-1} in the M_* -matched stacks and 11–13 km s^{-1} in the M_* +SFR-matched stacks. We therefore interpret the EW trend as an increase in absorbed velocity extent and/or velocity-dependent covering and emission filling, rather than as a purely LSF-driven profile-shape artifact. The profile widths in Figure 3 are still used only to guide the physical interpretation of the EW trend, not as a precision measurement of intrinsic velocity dispersion.

6. SUMMARY

We have used DESI DR1 stacked spectra to test whether stellar surface density is an independent empirical coordinate of Mg II cool-gas outflows in massive star-forming galaxies

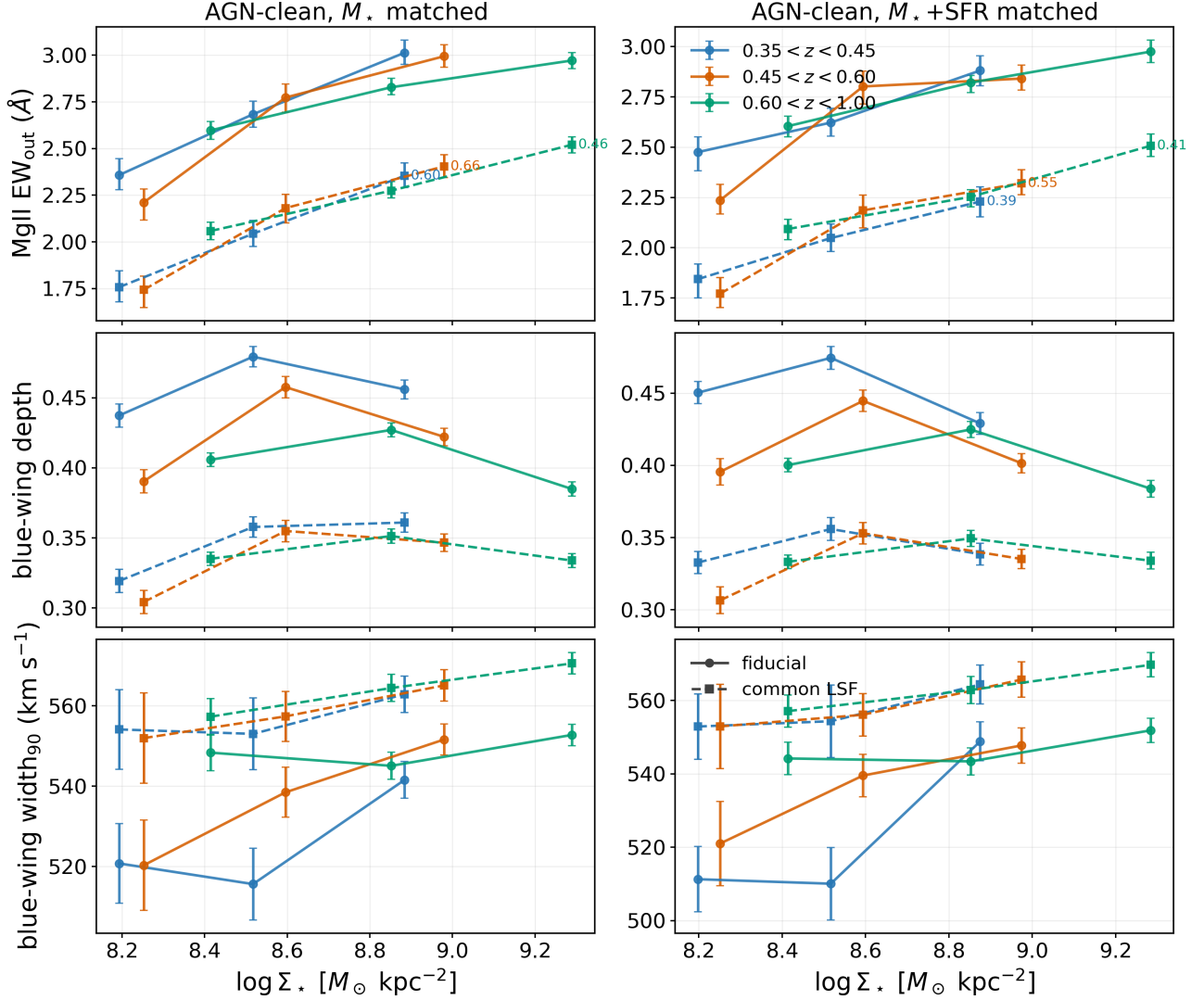


Figure 6. Test of the DESI LSF effect on the Mg II EW_{out} trend and on the profile-shape diagnostics used in Figure 3. Circles show the fiducial stacks used in the main analysis, while squares connected by dashed lines show stacks after all spectra are convolved to a common rest-frame LSF. The common-LSF stacks have smaller absolute EW_{out} , but the low-to-high- Σ_* increase remains in all three redshift bins and in both controlled samples. The qualitative profile interpretation also remains: the blue-wing depth is not a purely monotonic driver, whereas $width_{90}$ increases with Σ_* .

after controlling for stellar mass and SFR. Our main conclusions are:

1. In AGN-clean samples, Mg II EW_{out} increases monotonically with Σ_* in three redshift bins from $0.35 < z < 1.0$.
2. The trend persists in the fiducial sample matched in both M_* and line-SFR, demonstrating that compactness carries information beyond total stellar mass and our line-SFR proxy.
3. The profile-shape diagnostics suggest that the structural trend likely reflects changes in the absorbing velocity spread and/or effective covering fraction of the cool outflowing gas.

DESI therefore reveals stellar surface density as a measurable structural parameter in cool-gas feedback. The stacked spectra and tabulated EW_{out} measurements from this work provide a direct benchmark for models and future surveys that connect cool-gas covering fraction, absorbing velocity structure, and galaxy compactness.

1 This work uses data from DESI. We thank Hu Zou for provid-
 2 ing the DESI stellar-mass and emission-line catalog that en-
 3 ables the sample selection used here. YR acknowledges sup-
 4 ports from the CAS Pioneer Hundred Talents Program (Cat-
 5 egory B), the NSFC grants 12522302 and 12273037, and the
 6 USTC Research Funds of the Double First-Class Initiative.
 7 This work is supported by the China Manned Space Program
 8 with grant no. CMS-CSST-2025-A06 and CMS-CSST-2025-
 9 A08.

REFERENCES

- Arribas, S., Colina, L., Bellocchi, E., Maiolino, R., & Villar-Martin, M. 2014, *A&A*, 568, A14
- Baldwin, J. A., Phillips, M. M., & Terlevich, R. 1981, *PASP*, 93, 5
- Bordoloi, R., Lilly, S. J., Hardmeier, E., et al. 2014, *ApJ*, 794, 130
- Chevalier, R. A., & Clegg, A. W. 1985, *Nature*, 317, 44
- Chisholm, J., Tremonti, C. A., Leitherer, C., Chen, Y., Wofford, A., & Lundgren, B. 2015, *ApJ*, 811, 149
- Chisholm, J., Tremonti, C. A., Leitherer, C., Chen, Y., Wofford, A. 2016, *MNRAS*, 457, 3133
- Cicone, C., Maiolino, R., Sturm, E., et al. 2014, *A&A*, 562, A21
- Dekel, A., & Silk, J. 1986, *ApJ*, 303, 39
- Diamond-Stanic, A. M., Moustakas, J., Tremonti, C. A., et al. 2012, *ApJL*, 755, L26
- DESI Collaboration et al. 2022, *AJ*, 164, 207
- DESI Collaboration et al. 2026, *AJ*, 171, 285
- Dey, A., Schlegel, D. J., Lang, D., et al. 2019, *AJ*, 157, 168
- Erb, D. K., Quider, A. M., Henry, A. L., & Martin, C. L. 2012, *ApJ*, 759, 26
- Franx, M., van Dokkum, P. G., Förster Schreiber, N. M., Wuyts, S., Labbé, I., Toft, S. 2008, *ApJ*, 688, 770
- Heckman, T. M., Lehnert, M. D., Strickland, D. K., & Armus, L. 2000, *ApJS*, 129, 493
- Heckman, T. M., & Borthakur, S. 2016, *ApJ*, 822, 9
- Kauffmann, G., Heckman, T. M., Tremonti, C., et al. 2003, *MNRAS*, 346, 1055
- Kennicutt, R. C., Evans, N. J. 2012, *ARA&A*, 50, 531
- Kewley, L. J., Dopita, M. A., Sutherland, R. S., Heisler, C. A., & Trevena, J. 2001, *ApJ*, 556, 121
- Kewley, L. J., Groves, B., Kauffmann, G., & Heckman, T. 2006, *MNRAS*, 372, 961
- Kornei, K. A., Shapley, A. E., Martin, C. L., Coil, A. L., Lotz, J. M., Schiminovich, D., Bundy, K., Noeske, K. G. 2012, *ApJ*, 758, 135
- Martin, C. L. 2005, *ApJ*, 621, 227
- Martin, C. L., Shapley, A. E., Coil, A. L., et al. 2012, *ApJ*, 760, 127
- Martin, C. L., Shapley, A. E., Coil, A. L., Kornei, K. A., Murray, N., & Pancoast, A. 2013, *ApJ*, 770, 41
- Muratov, A. L., Kereš, D., Faucher-Giguère, C.-A., et al. 2015, *MNRAS*, 454, 2691
- Murray, N., Quataert, E., & Thompson, T. A. 2005, *ApJ*, 618, 569
- Naab, T., & Ostriker, J. P. 2017, *ARA&A*, 55, 59
- Newman, S. F., Genzel, R., Förster-Schreiber, N. M., et al. 2012, *ApJ*, 761, 43
- Oppenheimer, B. D., & Davé, R. 2006, *MNRAS*, 373, 1265
- Rong, Y., Zhu, K., Johnston, E. J., Zhang, H.-X., Cao, T., Puzia, T. H., Galaz, G. 2020, *ApJL*, 899, L12
- Rubin, K. H. R., Weiner, B. J., Koo, D. C., et al. 2010, *ApJ*, 719, 1503
- Rubin, K. H. R., Prochaska, J. X., Ménard, B., et al. 2011, *ApJ*, 728, 55
- Rubin, K. H. R., Prochaska, J. X., Koo, D. C., Phillips, A. C., Martin, C. L., Winstrom, L. O. 2014, *ApJ*, 794, 156
- Rupke, D. S., Veilleux, S., & Sanders, D. B. 2005, *ApJS*, 160, 115
- Sell, P. H., Tremonti, C. A., Hickox, R. C., et al. 2014, *MNRAS*, 441, 3417
- Shapley, A. E., Steidel, C. C., Pettini, M., & Adelberger, K. L. 2003, *ApJ*, 588, 65
- Somerville, R. S., & Davé, R. 2015, *ARA&A*, 53, 51
- Steidel, C. C., Erb, D. K., Shapley, A. E., et al. 2010, *ApJ*, 717, 289
- Tremonti, C. A., Moustakas, J., & Diamond-Stanic, A. M. 2007, *ApJL*, 663, L77
- Veilleux, S., Cecil, G., & Bland-Hawthorn, J. 2005, *ARA&A*, 43, 769
- Veilleux, S., Maiolino, R., Bolatto, A. D., & Aalto, S. 2020, *A&A Rev.*, 28, 2
- Weiner, B. J., Coil, A. L., Prochaska, J. X., et al. 2009, *ApJ*, 692, 187
- Wuyts, S., Förster Schreiber, N. M., van der Wel, A., et al. 2011, *ApJ*, 742, 96
- Yu, H., et al. 2025, *arXiv:2512.05584*
- Zou, H., et al. 2024, *ApJ*, 961, 173